



Microband-induced plasticity in a Ti-rich high-entropy alloy

S. Zherebtsov^a, N. Yurchenko^{a,*}, E. Panina^a, A. Tojibaev^a, M. Tikhonovsky^b,
G. Salishchev^a, N. Stepanov^a

^a Laboratory of Bulk Nanostructured Materials, Belgorod National Research University, Belgorod, 308015, Russia

^b National Science Center "Kharkov Institute of Physics and Technology" NAS of Ukraine, Kharkov, 61108, Ukraine



ARTICLE INFO

Article history:

Received 27 April 2020

Received in revised form

28 May 2020

Accepted 29 May 2020

Available online 3 June 2020

Keywords:

High-entropy alloys

Deformation

Microstructure evolution

Planar slip

Microbands

ABSTRACT

Microstructure evolution and mechanical behavior of an $\text{Al}_4\text{Mo}_4\text{Nb}_8\text{Ti}_{50}\text{Zr}_{34}$ high-entropy alloy were studied. In the as-cast condition, the alloy had a single-phase weakly B2 ordered bcc structure with a grain size of $100 \pm 50 \mu\text{m}$. The microstructure evolution during cold rolling to 90% thickness strain was initially associated with the development of substructure in the form of slip bands and then the formation of deformation bands propagating through several grains. Annealing of the cold-rolled alloy at $T \geq 700 \text{ }^\circ\text{C}$ resulted in the formation of a recrystallized microstructure with grain sizes varying from $\sim 6 \mu\text{m}$ after annealing at $600 \text{ }^\circ\text{C}$ to $\sim 250 \mu\text{m}$ at $1000 \text{ }^\circ\text{C}$. A small fraction of tiny oxides was observed in the alloy annealed at $700 \text{ }^\circ\text{C}$; the particles did not influence noticeably on the alloy properties. In spite of lack of work hardening in both the as-cast and recrystallized conditions, the alloy demonstrated the yield strength of 825–910 MPa and elongation to fracture of 11.5–15.2%. This behavior can be associated with strain localization due to the formation of dislocation microbands in the weakly B2 ordered bcc matrix.

© 2020 Elsevier B.V. All rights reserved.

1. Introduction

Activation of microband-induced plasticity (MBIP) in fcc metallic materials is usually related to a moderate level of the stacking fault energy ($\sim 90 \text{ mJ/m}^2$) [1]. The operation of this mechanism has been reported many times for high manganese steels [1–6], as well as for some fcc high entropy alloys (alloys based on five or more elements in nearly equiatomic concentrations, HEAs) [7–9]. The MBIP effect is associated with the formation of narrow planar shear zones confined by a dislocation wall on either side. MBIP (as well as transformation-induced plasticity/twinning-induced plasticity (TRIP/TWIP), which are observed at yet lower values of the stacking fault energy) usually results in the attaining of very high ductility together with high strength due to an exceptional strain hardening capacity.

Titanium alloys with the bcc crystalline lattice can also manifest various effects of plastic flow localization; however, these processes are usually not related to a certain value of the stacking fault energy [10]. Some recent papers reported the MBIP manifestation in bcc β -rich Ti alloys caused by phase transformation. Specifically, in a

series of Ti–Nb–Ta–Zr–O alloys, the development of the dislocation channels in planes depleted of ω particles occurred due to a local deformation-induced $\omega \rightarrow \beta$ transformation [11,12]. Dislocation movement was confined to widely spaced planes within which strain resistance was lower than that in the neighbor areas with a high density of the ω particles. Similar behavior was also found in oxygen-free alloys like Ti–25Nb–0.7Ta–2Zr [13] or Ti–3Al–8Mo–7V–3Cr [14].

Strain localization is also typical for gum metals, i.e., Ti-based alloys consisting elements of IVa and Va groups and 1.0–1.5 at.% of oxygen [15] (for example (at.%): Ti–20Nb–3.5Ta–3.4Zr–1.2O or Ti–12Ta–9Nb–3V–6Zr–1.5O). These alloys exhibit high tensile strength and ductility despite very weak work hardening; this unusual behavior was ascribed to the formation of the so-called giant faults due to the development of ideal bulk shear along certain crystallographic planes. Although dislocation motion in these alloys was initially supposed to be inhibited by Zr–O atoms clusters, later, dislocation and twinning activity was reported for gum metals [16–20]; besides, the giant faults' formation was also mainly ascribed to phase transformation effects [18,21,22].

Recently, another example of strain localization was also observed in an $\text{Al}_5\text{Nb}_{24}\text{Ti}_{40}\text{V}_5\text{Zr}_{26}$ HEA [23]. The alloy in a recrystallized condition had a partially (weakly) B2 ordered bcc matrix. During deformation, the formation of dislocation channels was

* Corresponding author. Laboratory of Bulk Nanostructured Materials, Belgorod National Research University, Pobeda 85, Belgorod, 308015, Russia.

E-mail address: yurchenko_nikita@bsu.edu.ru (N. Yurchenko).

observed in the microstructure [23]; the formation of these channels was ascribed to the matrix disordering. As a result, the alloy showed a mechanical behavior typical of gum metals (high strength and ductility, and lack of work hardening). These data suggest that the level of ordering (for example, due to different contents of Al [24,25]) can control the mechanical behavior of the HEA in a wide interval, and therefore this effect requires further investigation.

In this work, microstructure and mechanical properties of another Ti-rich Al-containing HEA $\text{Al}_4\text{Mo}_4\text{Nb}_8\text{Ti}_{50}\text{Zr}_{34}$ in the as-cast condition, during cold rolling and after recrystallization were studied. The effect of ordering on mechanical behavior and properties was established.

2. Materials and methods

The alloy with a nominal composition of $\text{Al}_4\text{Mo}_4\text{Nb}_8\text{Ti}_{50}\text{Zr}_{34}$ (the subscripts indicate the atomic percent of the corresponding element) was produced by arc melting of the elements in a low-pressure, high-purity argon atmosphere inside a water-cooled copper cavity. The purities of the elements were no less than 99.9 wt%. The size of the produced ingot was $\sim 12 \times 16 \times 50 \text{ mm}^3$. The chemical composition of the alloy measured by energy dispersive spectroscopy (EDS) closely corresponded to the nominal chemical composition (Table 1). The oxygen content was determined using the reduction-melting technique on a METEK-300/600 apparatus.

Rectangular samples measured $8 \times 12 \times 20 \text{ mm}^3$ were cut out by an electric discharge machine from the as-cast ingot to carry out thermomechanical processing. Unidirectional multipass rolling using a fixed rolling speed of 30 mm/s at room temperature to a thickness strain $\varepsilon_{\text{th}} = 10, 30, 60, \text{ or } 90\%$ was performed in air using a reduction per pass of approximately 0.1–0.2 mm. After rolling to the maximum thickness strain $\varepsilon_{\text{th}} = 90\%$, some specimens were further annealed at 600, 700, 800, 900, or 1000 °C for 1 h. Before annealing, the samples were sealed in vacuumed (10^{-2} torr) quartz tubes filled with titanium chips to prevent oxidation. After annealing, the specimens were water quenched. To obtain additional information on deformation mechanisms, some specimens in the as-cast state and after annealing at 1000 °C for 1 h were then rolled at room temperature to $\varepsilon_{\text{th}} = 7\%$.

The microstructure of the alloy was examined using X-ray diffraction (XRD), transmission (TEM), and scanning (SEM) electron microscopy and electron backscatter diffraction (EBSD) analysis. The XRD analysis was performed using a RIGAKU diffractometer with $\text{CuK}\alpha$ radiation. SEM specimens were prepared by careful mechanical polishing. SEM back-scattered electron (BSE) images of microstructures were obtained using a FEI Quanta 600 FEG microscope equipped with an EDS detector. SEM-BSE images were used for the evaluation of the average grain size through the linear intercept method with a Digimizer Image Analysis Software. The same software was used for the recrystallized fraction evaluation.

EBSD maps were obtained from the plane perpendicular to the transversal direction. Samples for EBSD were prepared by careful mechanical polishing. EBSD was conducted in a FEI Nova NanoSEM 450 field emission-gun scanning-electron microscope (FEG SEM)

equipped with a Hikari EBSD detector and a TSL OIM™ system version 6.0. This software was used to generate inverse pole figure (IPF) maps, on which high angle boundaries (HABs) are indicated with black lines and low angle boundaries (LABs) are indicated with white lines. Points having a low confidence index ($\text{CI} \leq 0.1$; depicted as black dots on the presented IPF maps) were excluded from the consideration.

TEM examinations were performed in a mid-thickness of the rolled specimens. Samples for the TEM analysis were prepared by a conventional twin-jet electropolishing at a temperature of $-35 \text{ }^\circ\text{C}$ and an applied voltage of 29.5 V in a mixture of 600 ml of methanol, 360 ml of butanol and 60 ml of perchloric acid. The TEM work was done using a JEOL JEM-2100 microscope, equipped with an EDS detector, at an accelerating voltage of 200 kV. At least five TEM bright-field images were used for the evaluation of the size and volume fraction of second phase particles with the aid of the Digimizer Image Analysis Software. The TEM-EDS detector was used for measuring the chemical composition of the second phase particles; at least ten individual measurements were carried out.

Specimens with the gauge dimensions of $6 \times 3 \times 1 \text{ mm}^3$ were used for mechanical tests under tension at a constant crosshead speed of 10^{-3} s^{-1} to fracture. The longitudinal axis of the specimens was aligned with the rolling direction. Elongation to fracture was determined by the measurements of spacing between marks designating the gauge length before and after the test. At least two samples in each condition were tested.

The microhardness of the specimens was examined using Vickers microhardness testing with a load of 0.2 kg. The hardness values were averaged over at least 20 individual measurements for each data point.

3. Results

3.1. As-cast structure

In the as-cast condition, the $\text{Al}_4\text{Mo}_4\text{Nb}_8\text{Ti}_{50}\text{Zr}_{34}$ alloy had a single-phase bcc structure with the lattice parameter $a = 0.3382 \pm 0.0002 \text{ nm}$ (Fig. 1a). The microstructure of the alloy consisted of rather equiaxed grains with an average size of $100 \pm 50 \mu\text{m}$ (Fig. 1b, Table 1). The chemical composition of the grains, determined using EDS, was close to the nominal one (Table 1). The measured oxygen content was found to be 0.4 at.%. TEM examination confirmed the bcc phase structure without any secondary phases (Fig. 1c). Meanwhile, selected area electron diffraction (SAED) patterns show the presence of weak superlattice (100) and (111) diffraction spots in [01-1] zone axis, suggesting weak B2 ordering of the bcc phase (insert in Fig. 1c; see a schematic representation of the SAED pattern for the [01-1]_{B2} zone axis). In addition, subtle streaks can be seen between the primary reflections.

3.2. Microstructure evolution during cold rolling

Inverse pole figure (IPF) maps of the as-cast $\text{Al}_4\text{Mo}_4\text{Nb}_8\text{Ti}_{50}\text{Zr}_{34}$ alloy after cold rolling (CR) to 10–90% thickness reduction

Table 1
Chemical compositions of the as-cast $\text{Al}_4\text{Mo}_4\text{Nb}_8\text{Ti}_{50}\text{Zr}_{34}$ alloy.

Elements, at.%		Al	Mo	Nb	Ti	Zr	O
Constituents		As-cast					
N ^o	Designation						
	Grains	4.7	2.1	8.3	50.5	34.4	-
	Alloy composition	4.2	2.2	7.9	50.4	34.9	0.4

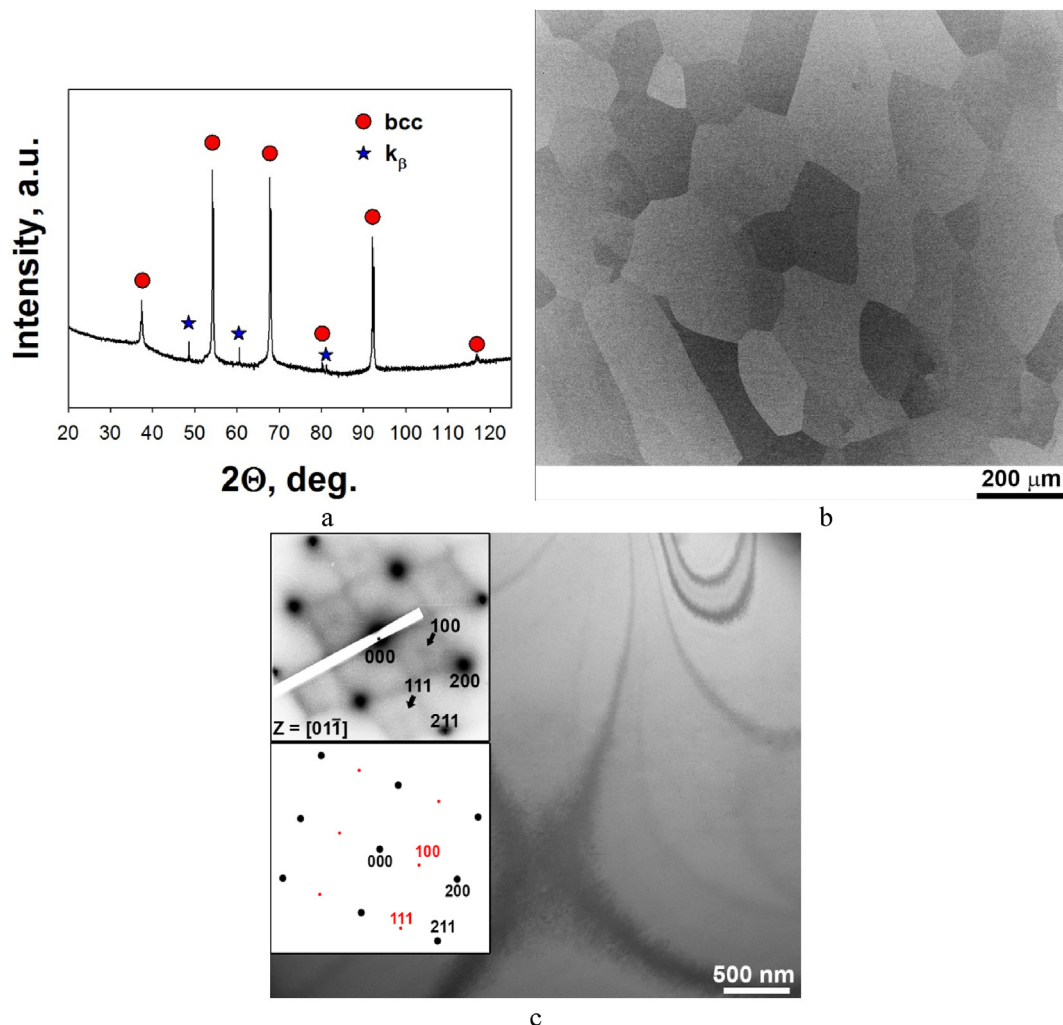


Fig. 1. XRD pattern (a) and microstructure (b, c) of the as-cast $\text{Al}_4\text{Mo}_4\text{Nb}_8\text{Ti}_{50}\text{Zr}_{34}$ alloy; b – SEM-BSE image; c – TEM bright-field image. Inserts in Fig. 1c show an experimental SAED pattern of the [01-1] zone axis of the B2 phase and its schematic representation.

(Fig. 2a–d) shows rather a heterogeneous character of the strain. Cold rolling to $\epsilon_{\text{th}} = 10\%$ resulted in the formation of a substructure comprising slip bands mainly, in some preferentially oriented for easy slip grains (Fig. 2a). After $\epsilon_{\text{th}} = 30\%$, the slip bands were observed in the majority of grains (Fig. 2b). At higher strains ($\epsilon_{\text{th}} = 60\%$), plastic deformation localized mainly within deformation bands, which could cross several grains (Fig. 2c and d). Meanwhile, a lot of relatively extensive areas not almost involved in strain can also be found. Further strain to $\epsilon_{\text{th}} = 90\%$ did not change the microstructure qualitatively, increasing, however, the fraction of the alloy occupied by the dislocation bands (due to which the EBSD map (not shown) contained a very low fraction of reliably determined dots with $\text{CI} > 0.1$; see for example the upper part of Fig. 2d). TEM examination (Fig. 2e) of the specimen deformed to the maximum thickness strain (90%) shows severe localization of plastic flow; a ring-type SAED pattern from the dislocation band suggests considerable microstructure fragmentation. In contrast, the SAED taken from an adjacent lower-strained area had a point-like pattern with subtle streaks; superlattice reflections were not recognized, however.

3.3. Effect of post-deformation annealing on structure

After cold rolling to $\epsilon_{\text{th}} = 90\%$, the alloy was annealed at

$T = 600\text{--}1000\text{ }^\circ\text{C}$ for 1 h. XRD analysis shows the single-phase bcc structure in the alloy after annealing; no peaks belonging to any other phase(s) were found (Fig. 3). The lattice parameter of the alloy did not change noticeably as a result of the annealing.

SEM examination showed only partial recrystallization after annealing at $600\text{ }^\circ\text{C}$ (the recrystallized volume V_{rec} was approximately 70%). Annealing at $T = 700\text{ }^\circ\text{C}$ resulted in the formation of a fully recrystallized homogeneous microstructure (Fig. 4a). An increase in the annealing temperature to $T \geq 800\text{ }^\circ\text{C}$ led to the microstructure coarsening (Fig. 4b). The grain size increased considerably from $\sim 6\text{ }\mu\text{m}$ at $600\text{ }^\circ\text{C}$ to $\sim 250\text{ }\mu\text{m}$ at $1000\text{ }^\circ\text{C}$ (Fig. 4c).

TEM examinations of specimens annealed at $700\text{ }^\circ\text{C}$ revealed (Fig. 5) an almost single-phase microstructure consisted of a bcc matrix and a very small fraction of tiny oxide particles with a tetragonal lattice (Fig. 5a). The particles enriched with Ti and Zr were mainly observed along some grain boundaries. The estimated volume fraction of the oxides and their average size were $\sim 1\%$ and $110 \pm 50\text{ nm}$, respectively. Second phase particles were not found in the recrystallized bcc matrix after annealing at $1000\text{ }^\circ\text{C}$ (Fig. 5b); however it can be associated with very large grains ($250\text{ }\mu\text{m}$) due to which grain boundaries (the most expected site of the particles nucleation) were rarely observed at TEM images. It should be noted, that both superlattice reflections and streaks between the primary reflections were scarcely visible at SAED patterns (inserts in Fig. 5a

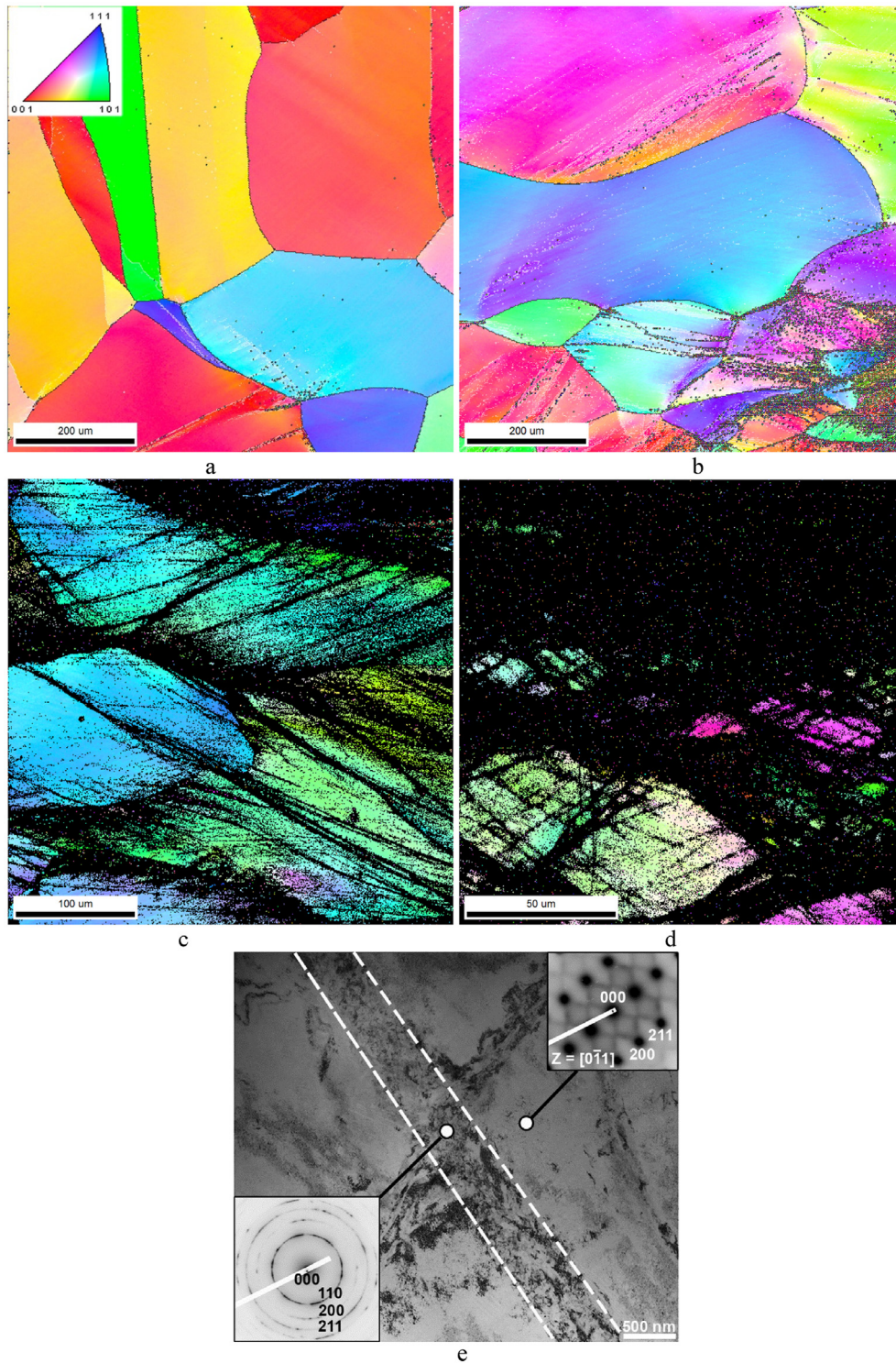


Fig. 2. Microstructure of the $\text{Al}_4\text{Mo}_4\text{Nb}_8\text{Ti}_{50}\text{Zr}_{34}$ alloy after CR to strain of 10% (a), 30% (b), 60% (c), 90% (d, e); a-d – IPF maps; e – TEM bright-field image. The rolling direction is horizontal.

and b) taken from the bcc phase of the specimens annealed at both temperatures (700 and 1000 °C).

3.4. Mechanical properties

Mechanical properties of the $\text{Al}_4\text{Mo}_4\text{Nb}_8\text{Ti}_{50}\text{Zr}_{34}$ alloy in the as-cast, cold-rolled, and annealed conditions were evaluated using

both microhardness measurement and tensile tests. The microhardness of the as-cast alloy was $255 \pm 5 \text{ HV}_{0.2}$; this value did not change significantly after $\epsilon_{\text{th}} = 10\%$ (Fig. 6a). However, further cold rolling led to an almost linear increase in the microhardness up to $335 \pm 5 \text{ HV}_{0.2}$ after 90% of CR. It is worth noting, however, that the overall increment in the hardness after $\epsilon_{\text{th}} = 90\%$ was relatively low (~30%). Post-deformation annealing at $T \geq 700$ °C resulted in a

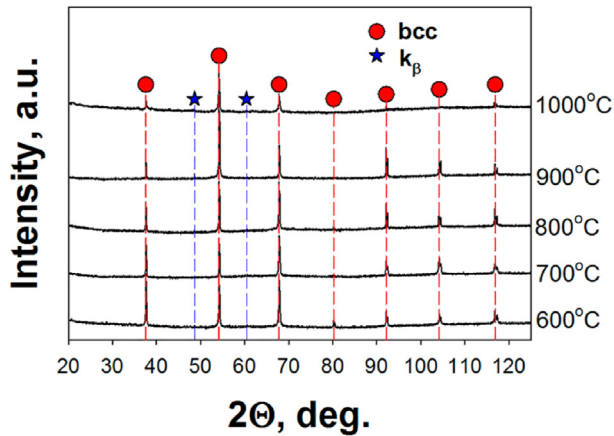


Fig. 3. XRD patterns of the $\text{Al}_4\text{Mo}_4\text{Nb}_8\text{Ti}_{50}\text{Zr}_{34}$ alloy after CR and further annealing at 600–1000 °C for 1 h.

decrease in the microhardness value to the as-cast level (Fig. 6b). Annealing at 600 °C gave a little higher value of $\sim 270 \text{ HV}_{0.2}$ (most probably due to the incomplete recrystallization, see Fig. 4a).

Both the true and engineering stress – strain tensile curves of the cold-rolled alloy (Fig. 6c and d) was quite typical for the deformed conditions and showed fast strain localization after a short stage of strengthening. The yield strength and elongation to fracture of the cold-rolled alloy were found to be 1330 MPa and

7.5%, respectively (Table 2). Both the initial as-cast and recrystallized alloy demonstrated quite similar curves with a slight decrease in flow stress just after the yield point (the strain hardening coefficient was close to zero for both conditions) due to early necking. However, even after the strain localization, the recrystallized specimens showed both quite a high ductility (~ 11 –15%) and the presence of a quasi-steady flow stage.

To determine the main operating deformation mechanisms, specimens of the alloy in the as-cast condition and after recrystallization at 1000 °C were additionally cold rolled to a small thickness strain $\epsilon_{\text{th}} = 7\%$. Note, the similarity of both cold-rolled and tensile tested deformation structures for recrystallized at 1000 °C state and numerous failed attempts to prepare foils of the as-cast tensile specimens resulted in favor of the cold-rolled scheme for both conditions in the sake of comparability. The similarity in deformation behavior between these two conditions is quite obvious (Fig. 7). Small deformation of both the as-cast and recrystallized conditions was associated with the development of planar slip resulting in the formation of a grid-like structure due to crossing dislocation microbands (Fig. 7a and b). Dislocations were quite rarely observed outside of the dislocation microbands. In addition, SAED, taken from an area not almost involved in deformation, still showed the signs of ordering (superlattice reflections between the primary reflections; the lower-left insert in Fig. 7a) in contrast to the SAED pattern obtained from the dislocation microbands, where superlattice reflections were not recognized (the upper-left insert in Fig. 7a). Similar phenomena were observed in the recrystallized conditions.

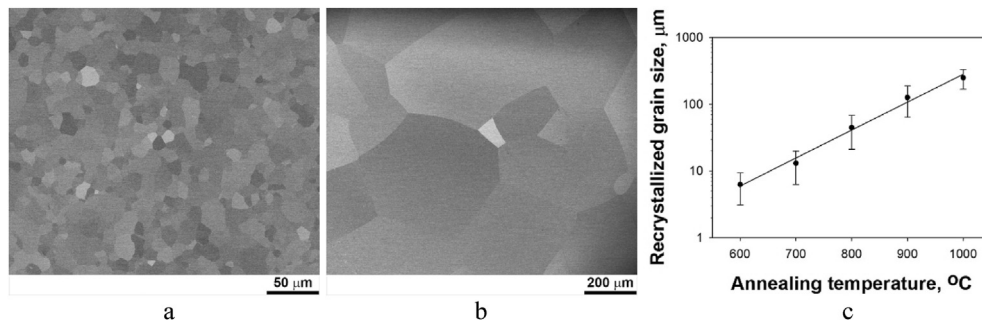


Fig. 4. SEM-BSE images the $\text{Al}_4\text{Mo}_4\text{Nb}_8\text{Ti}_{50}\text{Zr}_{34}$ alloy after cold-rolling to $\epsilon_{\text{th}} = 90\%$ and further annealing at 700 (a) or 1000 °C (b) and the semi-logarithmic dependence of grain size on annealing temperature (c).

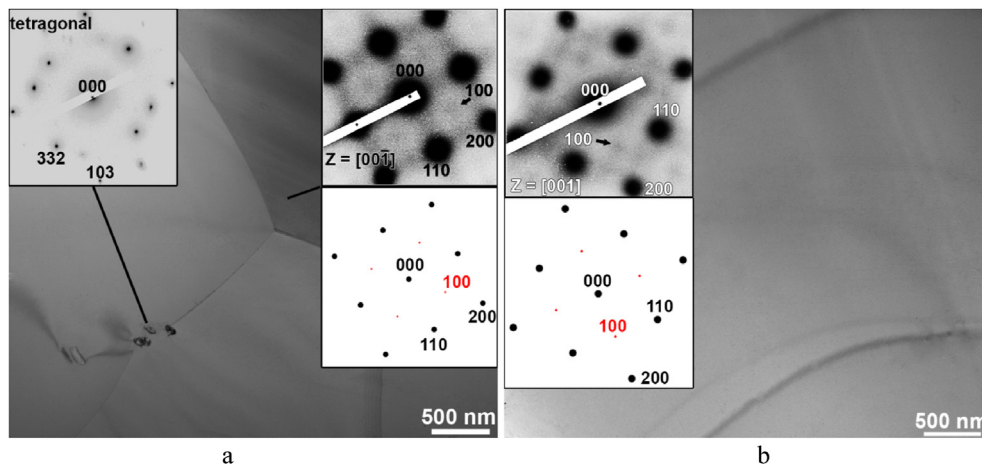


Fig. 5. TEM bright-field images of the $\text{Al}_4\text{Mo}_4\text{Nb}_8\text{Ti}_{50}\text{Zr}_{34}$ alloy recrystallized at 700 (a) or 1000 °C (b) for 1 h. Inserts show experimental SAED patterns of the $\langle 001 \rangle$ zone axes of the B2 phase and their schematic representation.

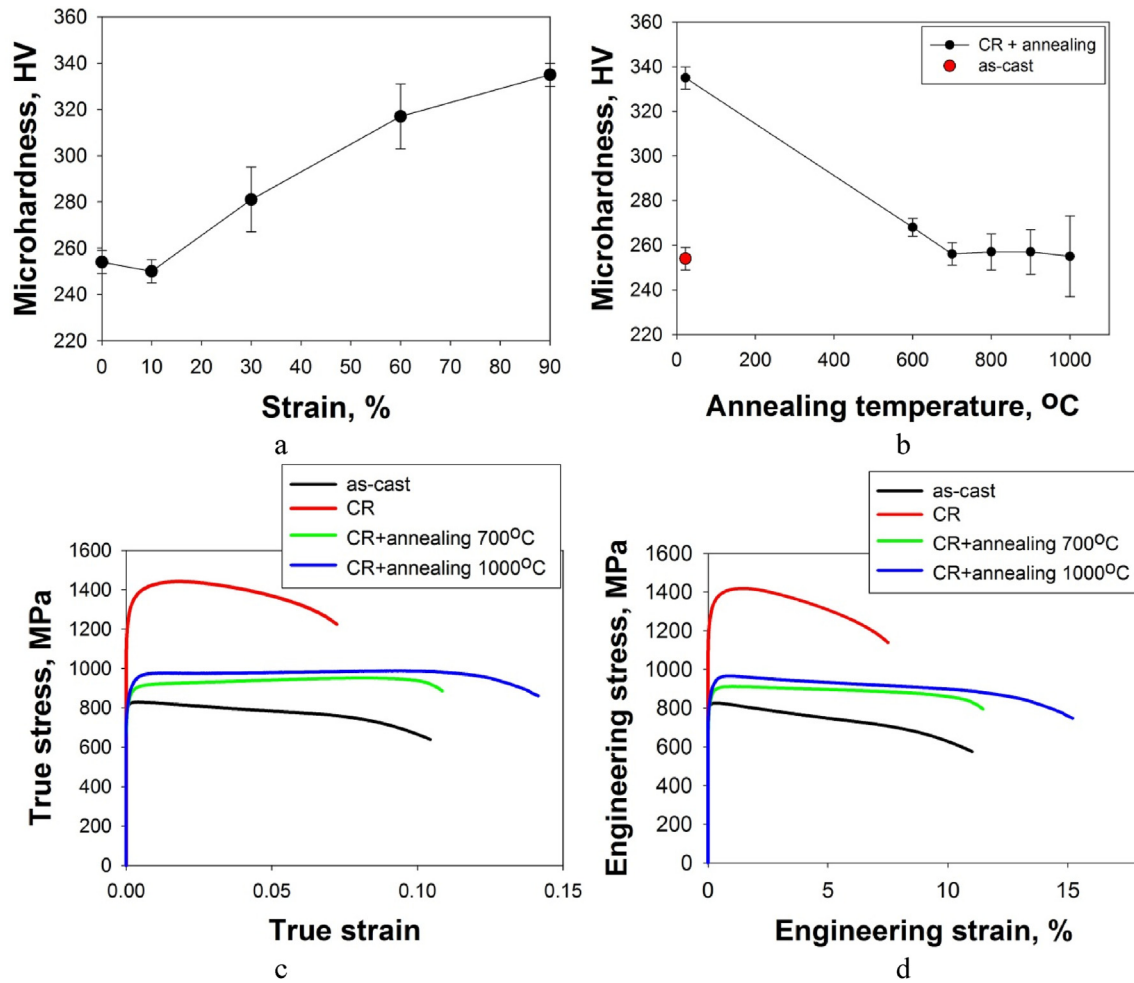


Fig. 6. Mechanical behavior of the $\text{Al}_4\text{Mo}_4\text{Nb}_8\text{Ti}_{50}\text{Zr}_{34}$ alloy in different conditions: microhardness as a function of strain during cold rolling (a); microhardness evolution during post-deformation annealing at 600–1000 °C for 1 h after CR to $\epsilon_{th} = 90\%$ (b); true (c) and engineering (d) stress-strain curves.

Table 2

Tensile mechanical characteristics^a of the $\text{Al}_4\text{Mo}_4\text{Nb}_8\text{Ti}_{50}\text{Zr}_{34}$ alloy in the as-cast state, after CR, and CR + annealing at 700 °C for 1 h.

Condition	YS, MPa	UTS, MPa	TE, %
As-cast	825	825	11.0
CR	1330	1420	7.5
CR + annealing at 700 °C, 1h	880	910	11.5
CR + annealing at 1000 °C, 1h	910	965	15.2

^a YS – yield strength, UTS – ultimate tensile strength, TE – tensile elongation.

4. Discussion

The program $\text{Al}_4\text{Mo}_4\text{Nb}_8\text{Ti}_{50}\text{Zr}_{34}$ alloy exhibited two special features: (i) the stable weakly B2 ordered bcc structure survived in general (except for the areas of plastic flow localization) even after large cold rolling to $\epsilon_{th} = 90\%$ and (ii) the unusual mechanical behavior typical of gum metals, i.e., high yield strength, low work hardening, and reasonable ductility. The ‘classical’ approach suggests that the unique characteristics of gum metals can be ascribed to pronounced flow localization along certain crystallographic planes with a low resistance to shear. This behavior is supposed to be caused by low stability of the β phase on the one hand and high critical shear stress for dislocation motion due to the presence of a high density of nano-sized ZrO or the ω phase pinning clusters [26]

on the other hand.

In our case, dislocation activity was rather high; the formation of dislocation microbands implies that the critical shear stress for dislocation glide is lower than the resistance to shear along any crystallographic plane. At the same time, weak B2 ordering can contribute to the formation of the dislocation microbands (Fig. 7). An accepted concept of the planar slip suggests that the leading dislocation gliding along an atomic plane destroys obstacles (ordering in our case) and thereby decreases the energy barrier for following dislocations [27]. Once a certain quantity of the obstacles-free slip bands are formed, further deformation develops with relatively low strain hardening that is in good agreement with the present results (Fig. 6c). It is worth noting that some disordered bcc HEAs like the equiatomic HfNbTaTiZr and its derivatives can also show a tendency to strain localization via the kink bands formation [28–31].

The B2 ordering found in the program $\text{Al}_4\text{Mo}_4\text{Nb}_8\text{Ti}_{50}\text{Zr}_{34}$ alloy has two characteristic features. First, judging by the dimness or complete absence of the superlattice reflections in the SAED (Figs. 1c, 2e and 5, and 7) or XRD patterns (Figs. 1a and 3), respectively, it can be concluded that the degree of order S is rather low (the S value can vary from 0 when atomic species are randomly distributed between the lattice sites to 1 if atoms of each sort can be found in certain sublattice sites only). It should be noted, however, that even revealing the fact of ordering, let alone the experimental

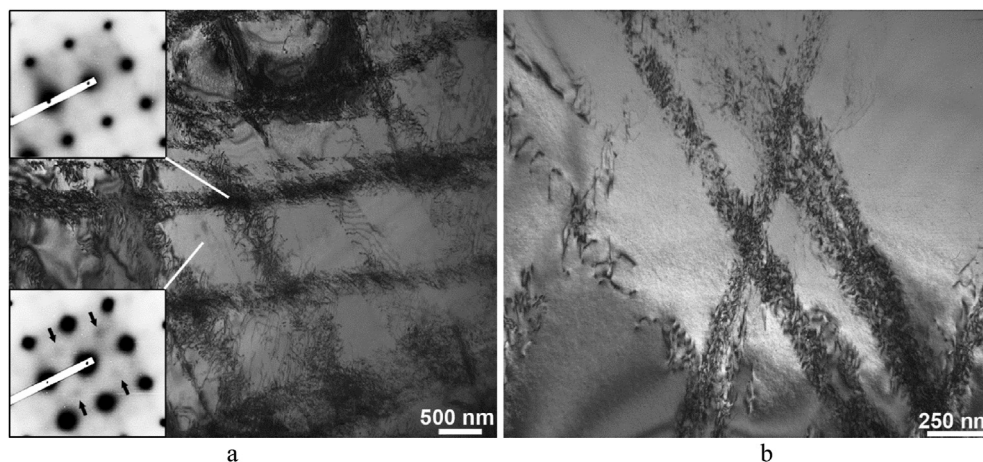


Fig. 7. TEM-bright field images of the $\text{Al}_4\text{Mo}_4\text{Nb}_5\text{Ti}_{50}\text{Zr}_{34}$ alloy CR to 7% thickness strain in the as-cast state (a) and recrystallized at 1000 °C (b) for 1 h. Arrows indicate the (100) superlattice reflections.

determination of the S value, is a complicated task, especially for such a complex, multicomponent alloy [32–35]. Second, the S value varies through the bulk of the material; the superlattice reflections are visible in the non-deformed areas ($S > 0$) and are not recognized in the deformation bands ($S = 0$) (Figs. 2e and 7a). In a simplified form, the microstructure in the as-cast and recrystallized conditions can be considered as that consisted of areas with various degree of order [33], and plastic deformation more readily occurs in the “less ordered” areas which act as precursors for deformation bands. However, further studies are required to prove these assumptions.

The stress-strain curves demonstrate lower both strength and ductility of the as-cast specimens in comparison to those of the recrystallized alloy (Fig. 6c). These differences can also be caused by variations in the S value. One can suggest that the more obvious superlattice reflexes in the as-cast alloy (compare Figs. 1c and 5) imply a higher degree of order and, as a consequence, higher strength of the alloy. However, an increase in S does not necessarily result in higher strength and lower ductility. For example, it was shown in Ref. [36] with respect to a number of intermetallic compositions that, at room temperature, the disordered state is stronger than the ordered one. This behavior was ascribed to a transition from the interaction of unit dislocations with a weakly ordered lattice to the interaction of superdislocations with a nearly perfectly ordered lattice [36,37]. Since the spacing between dislocation pairs, constituting superlattice dislocations, is inversely proportional to S^2 [35], a very fast increase in the spacing with decreasing S occurs, resulting in the independent glide of each unit dislocation at large separations. In materials with low S , slipping unit dislocations can leave antiphase boundary trails, thereby forming wrong bonds and increasing strength by analogy to that observed in the case of short-range order. In contrast, superlattice dislocations in conditions with high S do not create wrong bonds behind, resulting in some decrease in strength as the proportion of superlattice dislocations increases [36,37]. In addition, in alloys with low S , (or with short-range ordering) planar slip tends to delocalize, forming a thin 3D zone due to cross-slip of the screw components to adjacent prismatic planes [23,28,38] that can result in some increase in ductility. The presence of oxygen in the program alloy has possibly a somewhat similar influence on mechanical behavior due to the ZrO clusters formation, which might act as short-range order domains [15].

Besides, it can be suggested that oxygen in the program alloy is mainly in the solid solution in the as-cast and annealed at 1000 °C

conditions, while the formation of oxides enriched with Ti and Zr was observed after recrystallization treatment at 700 °C (Fig. 5a). Due to a very low amount of these particles, their contribution to the grain coarsening kinetics was negligible (Fig. 4). However, the formation of oxides resulted in some decrease in the content of oxygen in the solid solution, due to which strength of the alloy was 30–50 MPa lower than that observed after annealing at 1000 °C (Table 2, Fig. 6c) despite the smaller grain size (and therefore a higher contribution of the Hall-Petch strengthening).

The obtained results can be quite interesting in the context of prediction of structure/properties relation in Ti-rich HEAs. Traditionally, the stability of the β phase in titanium alloys is associated with the molybdenum equivalent (Mo_{eq}). This criterion can be used to divide titanium alloys into three groups (α , $\alpha+\beta$, and β) and allows rough predicting the dominant deformation mechanism (dislocation slip, twinning or phase transformation) [39]. However, a high fraction of Al in many HEAs decreases Mo_{eq} to very low (even negative) values making impossible the use of this criterion in the case of Ti-rich HEAs. For example, the molybdenum equivalent of the program alloys was found to be 7.2 [40]; this value corresponds to the $\alpha+\beta$ domain while the alloy has a stable bcc (B2) lattice. This observation suggests that not all approaches established for Ti alloys can readily be applied to Ti-rich HEAs.

At the end of the last century, Morinaga with co-authors proposed the $\overline{B}_o - \overline{M}_d$ approach (\overline{B}_o is the bond order and \overline{M}_d is the metal d-orbital energy level) for predicting the β phase stability in titanium alloys [41]. The position of a titanium alloy on the $\overline{B}_o - \overline{M}_d$ map (and therefore, the dominant deformation mechanism) is associated with the alloy composition. For example, TRIP/TWIP effect was reported for the first time in a Ti–12Mo alloy developed using the $\overline{B}_o - \overline{M}_d$ map [42,43]. Now, the semi-empirical “d-electron alloy design” approach is considered as a reliable guide for designing titanium alloys with TRIP/TWIP effects. However, it is not quite clear if the $\overline{B}_o - \overline{M}_d$ approach is valid for (i) predicting the MBIP effect and (ii) can be used for Ti-rich high-entropy alloys.

Therefore, we have plotted a number of Ti alloys with MBIP effect, Ti-based gum metals, and Ti-rich HEAs with either MBIP or TRIP effect at the $\overline{B}_o - \overline{M}_d$ map (Fig. 8). Quite unexpectedly, two groups of Ti-based alloys (MBIP Ti alloys and gum metals), which demonstrate flow localization during deformation, were also located at (or very close to) the $M_s = \text{RT}$ line. This finding suggests that this ‘d-electron alloy design’ approach can be used to predict some other effect of plastic flow localization caused by low stability

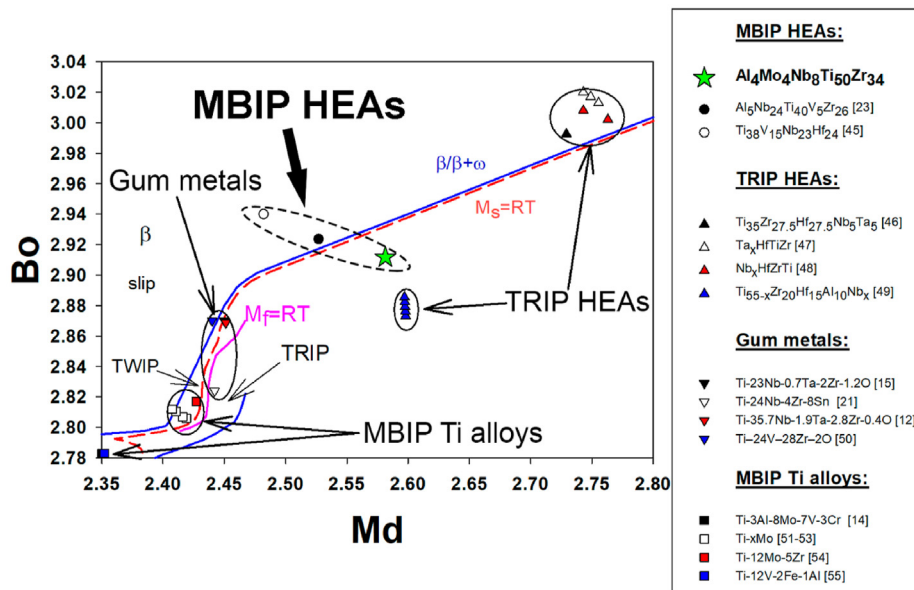


Fig. 8. Positions of the program $\text{Al}_4\text{Mo}_4\text{Nb}_8\text{Ti}_{50}\text{Zr}_{34}$ alloy, some MBIP [23,45] and TRIP Ti-rich HEAs [46–49], gum metals [12,15,21,50], and MBIP Ti alloys [14,51–55] on the $\overline{B}_0 - \overline{M}_d$ map.

of the bcc lattice, including the formation of deformation bands or giant faults. It should be noted that although the exact \overline{B}_0 and \overline{M}_d values were assigned for gum metals (\overline{B}_0 should be ~ 2.87 and $\overline{M}_d \sim 2.45$ eV) in the very first report [15] to warrant necessary β phase stability [44], the exact underlying physical mechanism of this phenomenon is not quite clear so far.

Meanwhile, the program $\text{Al}_4\text{Mo}_4\text{Nb}_8\text{Ti}_{50}\text{Zr}_{34}$ alloy was located slightly below the $M_s = \text{RT}$ line (Fig. 8), extended for Ti-rich HEAs in accordance with [46]. Judging by this map, the program alloy could demonstrate a TRIP effect during deformation; however, neither deformation twinning nor deformation-induced phase transformation was observed in the deformed microstructure of the alloy. Similarly, the MBIP effect was observed in another weakly B2 ordered $\text{Al}_5\text{Nb}_{24}\text{Ti}_{40}\text{V}_5\text{Zr}_{26}$ HEA [23] (located slightly above the $M_s = \text{RT}$ line). In a $\text{Ti}_{38}\text{V}_{15}\text{Nb}_{23}\text{Hf}_{24}$ alloy, located almost at the $M_s = \text{RT}$ line, the MBIP effect was associated with the formation of channels devoid of V-rich bcc precipitates [45]. This type of behavior resembled some other Ti alloys with the MBIP effect [11–14]. The position of the Ti-rich HEAs with the MBIP effect on the $\overline{B}_0 - \overline{M}_d$ diagram suggest its usefulness for the search of new HEAs with advanced properties. For instance, the strength-ductility characteristics of the program $\text{Al}_4\text{Mo}_4\text{Nb}_8\text{Ti}_{50}\text{Zr}_{34}$ alloy (Table 2) can be favorably compared with some other bcc HEAs [56–59]. However, it is worth to mention that Ti-rich HEAs with TRIP effect were scattered on this diagram with respect to the $M_s = \text{RT}$ line position. Most probably, this uncertainty is caused by insufficient amount of the experimental data used to extrapolate the line from the well-studied Ti alloys region to the poorly unexplored HEAs area with much higher \overline{B}_0 and \overline{M}_d values. Additional experimental work is required therefore to establish the exact position of the $M_s = \text{RT}$ line in a wide concentration range to make it more reliable instrument for the advanced HEA development.

5. Conclusions

Microstructure and mechanical behavior of an $\text{Al}_4\text{Mo}_4\text{Nb}_8\text{Ti}_{50}\text{Zr}_{34}$ high-entropy alloy were analyzed. Following conclusions were drawn:

- 1 In the as-cast condition, the alloy had a single bcc phase structure with grains of $100 \pm 50 \mu\text{m}$; SAED patterns showed weak ordering of the crystalline lattice. Cold rolling to a thickness strain $\epsilon_{\text{th}} = 90\%$ and subsequent annealing at $600\text{--}1000^\circ\text{C}$ resulted in recrystallization of the alloy. The grain size of the recrystallized alloy was $\sim 6 \mu\text{m}$ after annealing at 600°C and $\sim 250 \mu\text{m}$ at 1000°C . After annealing at 700°C , Ti- and Zr-rich oxides were found in the microstructure; the fraction and the average size of the particles were $\sim 1\%$ and $110 \pm 50 \text{ nm}$, respectively. Weak ordering of the matrix phase maintained after the annealing.
- 2 Deformation of the alloy was associated with the formation of dislocation microbands within which the crystalline lattice was found to be disordered. Due to this strain localization, the alloy shows rather high yield strength ($\sim 900 \text{ MPa}$) and moderate ductility (11–15%) in recrystallized conditions with very low strain hardening capacity.

Data availability statement

The raw/processed data required to reproduce these findings cannot be shared at this time as the data also forms part of an ongoing study.

CRediT authorship contribution statement

S. Zhrebtsov: Conceptualization, Supervision, Writing - original draft. **N. Yurchenko:** Methodology, Investigation, Visualization, Data curation, Formal analysis, Writing - review & editing. **E. Panina:** Formal analysis, Investigation. **A. Tojibaev:** Investigation. **M. Tikhonovsky:** Resources. **G. Salishchev:** Project administration, Funding acquisition. **N. Stepanov:** Validation, Writing - review & editing.

Declaration of competing interest

The authors declare that they have no known competing financial interests or personal relationships that could have

appeared to influence the work reported in this paper.

Acknowledgement

The authors gratefully acknowledge the financial support from the Russian Science Foundation Grant no.19-79-30066. The authors are grateful to the personnel of the Joint Research Center, «Technology and Materials», Belgorod National Research University, for their assistance with the instrumental analysis.

Appendix A. Supplementary data

Supplementary data to this article can be found online at <https://doi.org/10.1016/j.jallcom.2020.155868>.

References

- [1] J.D. Yoo, K.T. Park, Microband-induced plasticity in a high Mn–Al–C light steel, *Mater. Sci. Eng. A* 496 (2008) 417–424, <https://doi.org/10.1016/j.msea.2008.05.042>.
- [2] J.D. Yoo, S.W. Hwang, K.T. Park, Origin of extended tensile ductility of a Fe–28Mn–10Al–1C steel, *Metall. Mater. Trans. A Phys. Metall. Mater. Sci.* 40 (2009) 1520–1523, <https://doi.org/10.1007/s11661-009-9862-9>.
- [3] I. Gutierrez-Urrutia, D. Raabe, Microbanding mechanism in an Fe–Mn–C high-Mn twinning-induced plasticity steel, *Scripta Mater.* 69 (2013) 53–56, <https://doi.org/10.1016/j.scriptamat.2013.03.010>.
- [4] C. Haase, C. Zehnder, T. Ingendahl, A. Bikar, F. Tang, B. Hallstedt, W. Hu, W. Bleck, D.A. Molodov, On the deformation behavior of κ -carbide-free and κ -carbide-containing high-Mn light-weight steel, *Acta Mater.* 122 (2017) 332–343, <https://doi.org/10.1016/j.actamat.2016.10.006>.
- [5] E. Welsch, D. Ponge, S.M. Hafez Haghghat, S. Sandlöbes, P. Choi, M. Herbig, S. Zaeferrer, D. Raabe, Strain hardening by dynamic slip band refinement in a high-Mn lightweight steel, *Acta Mater.* 116 (2016) 188–199, <https://doi.org/10.1016/j.actamat.2016.06.037>.
- [6] K.T. Park, Tensile deformation of low-density Fe–Mn–Al–C austenitic steels at ambient temperature, *Scripta Mater.* 68 (2013) 375–379, <https://doi.org/10.1016/j.scriptamat.2012.09.031>.
- [7] D.B. Miracle, O.N. Senkov, A critical review of high entropy alloys and related concepts, *Acta Mater.* 122 (2017) 448–511, <https://doi.org/10.1016/j.actamat.2016.08.081>.
- [8] Z. Wang, I. Baker, Z. Cai, S. Chen, J.D. Poplawsky, W. Guo, The effect of interstitial carbon on the mechanical properties and dislocation substructure evolution in Fe₄₀Ni₁₁Mn₃₄Al₇Cr₆ high entropy alloys, *Acta Mater.* 120 (2016) 228–239, <https://doi.org/10.1016/j.actamat.2016.08.072>.
- [9] Z. Wang, H. Bei, I. Baker, Microband induced plasticity and the temperature dependence of the mechanical properties of a carbon-doped FeNiMnAlCr high entropy alloy, *Mater. Char.* 139 (2018) 373–381, <https://doi.org/10.1016/j.matchar.2018.03.017>.
- [10] G.H. Zhao, X. Xu, D. Dye, P.E.J. Rivera-Díaz-del-Castillo, Microstructural evolution and strain-hardening in TWIP Ti alloys, *Acta Mater.* 183 (2020) 155–164, <https://doi.org/10.1016/j.actamat.2019.11.009>.
- [11] M.J. Lai, C.C. Tasan, D. Raabe, Deformation mechanism of ω -enriched Ti–Nb-based gum metal: dislocation channeling and deformation induced ω – β transformation, *Acta Mater.* 100 (2015) 290–300, <https://doi.org/10.1016/j.actamat.2015.08.047>.
- [12] J.L. Zhang, C.C. Tasan, M.J. Lai, D. Yan, D. Raabe, Partial recrystallization of gum metal to achieve enhanced strength and ductility, *Acta Mater.* 135 (2017) 400–410, <https://doi.org/10.1016/j.actamat.2017.06.051>.
- [13] M.J. Lai, T. Li, D. Raabe, ω phase acts as a switch between dislocation channeling and joint twinning- and transformation-induced plasticity in a metastable β titanium alloy, *Acta Mater.* 151 (2018) 67–77, <https://doi.org/10.1016/j.actamat.2018.03.053>.
- [14] S. Sadeghpour, S.M. Abbasi, M. Morakabati, L.P. Karjalainen, Effect of dislocation channeling and kink band formation on enhanced tensile properties of a new beta Ti alloy, *J. Alloys Compd.* 808 (2019) 151741, <https://doi.org/10.1016/j.jallcom.2019.151741>.
- [15] T. Saito, T. Furuta, J.-H. Hwang, S. Kuramoto, K. Nishino, N. Suzuki, R. Chen, A. Yamada, K. Ito, Y. Seno, T. Nonaka, H. Ikehata, N. Nagasako, C. Iwamoto, Y. Ikuhara, T. Sakuma, Multifunctional alloys obtained via a dislocation-free plastic deformation mechanism, *Science* 300 (2003) 464–467, <https://doi.org/10.1126/science.1081957>.
- [16] R.J. Talling, R.J. Dashwood, M. Jackson, D. Dye, On the mechanism of super-elasticity in Gum metal, *Acta Mater.* 57 (2009) 1188–1198, <https://doi.org/10.1016/j.actamat.2008.11.013>.
- [17] T. Li, J.W. Morris, N. Nagasako, S. Kuramoto, D.C. Chrzan, “Ideal” engineering alloys, *Phys. Rev. Lett.* 98 (2007) 105503, <https://doi.org/10.1103/PhysRevLett.98.105503>.
- [18] M. Tahara, H.Y. Kim, T. Inamura, H. Hosoda, S. Miyazaki, Lattice modulation and superelasticity in oxygen-added β -Ti alloys, *Acta Mater.* 59 (2011) 6208–6218, <https://doi.org/10.1016/j.actamat.2011.06.015>.
- [19] Y. Yang, P. Castany, M. Cornen, F. Prima, S.J. Li, Y.L. Hao, T. Gloriant, Characterization of the martensitic transformation in the superelastic Ti–24Nb–4Zr–8Sn alloy by in situ synchrotron X-ray diffraction and dynamic mechanical analysis, *Acta Mater.* 88 (2015) 25–33, <https://doi.org/10.1016/j.actamat.2015.01.039>.
- [20] Q. Liang, Y. Zheng, D. Wang, Y. Hao, R. Yang, Y. Wang, H.L. Fraser, Nano-scale structural non-uniformities in gum like Ti–24Nb–4Zr–8Sn metastable β -Ti alloy, *Scripta Mater.* 158 (2019) 95–99, <https://doi.org/10.1016/j.scriptamat.2018.08.043>.
- [21] Y. Yang, P. Castany, M. Cornen, F. Prima, S.J. Li, Y.L. Hao, T. Gloriant, Characterization of the martensitic transformation in the superelastic Ti–24Nb–4Zr–8Sn alloy by in situ synchrotron X-ray diffraction and dynamic mechanical analysis, *Acta Mater.* 88 (2015) 25–33, <https://doi.org/10.1016/j.actamat.2015.01.039>.
- [22] Q. Liang, Y. Zheng, D. Wang, Y. Hao, R. Yang, Y. Wang, H.L. Fraser, Nano-scale structural non-uniformities in gum like Ti–24Nb–4Zr–8Sn metastable β -Ti alloy, *Scripta Mater.* 158 (2019) 95–99, <https://doi.org/10.1016/j.scriptamat.2018.08.043>.
- [23] S. Zhrebtsov, N. Yurchenko, E. Panina, M. Tikhonovsky, N. Stepanov, Gum-like mechanical behavior of a partially ordered Al₅Nb₂₄Ti₄₀V₅Zr₂₆ high entropy alloy, *Intermetallics* 116 (2020) 106652, <https://doi.org/10.1016/j.intermet.2019.106652>.
- [24] N.Y. Yurchenko, N.D. Stepanov, S. V. Zhrebtsov, M.A. Tikhonovsky, G.A. Salishchev, Structure and mechanical properties of B2 ordered refractory AlNbTiVZr_x (x=0–1.5) high-entropy alloys, *Mater. Sci. Eng. A* 704 (2017) 82–90, <https://doi.org/10.1016/j.msea.2017.08.019>.
- [25] S. Laube, H. Chen, A. Kauffmann, S. Schellert, F. Müller, B. Gorr, J. Müller, B. Butz, H.J. Christ, M. Heilmair, Controlling crystallographic ordering in Mo–Cr–Ti–Al high entropy alloys to enhance ductility, *J. Alloys Compd.* 823 (2020) 153805, <https://doi.org/10.1016/j.jallcom.2020.153805>.
- [26] M. Besse, P. Castany, T. Gloriant, Mechanisms of deformation in gum metal TNiZr–O and TNiZr titanium alloys: a comparative study on the oxygen influence, *Acta Mater.* 59 (2011) 5982–5988, <https://doi.org/10.1016/j.actamat.2011.06.006>.
- [27] R.E. Smallman, Ray J. Bishop, *Metals and Materials: Science, Processes, Applications*, Butterworth-Heinemann, 1995.
- [28] J.-P. Couzinié, L. Liliensten, Y. Champion, G. Dirras, L. Perrière, I. Guillot, On the room temperature deformation mechanisms of a TiZrHfNbTa refractory high-entropy alloy, *Mater. Sci. Eng. A* 645 (2015) 255–263, <https://doi.org/10.1016/j.msea.2015.08.024>.
- [29] S. Zhrebtsov, N. Yurchenko, D. Shaysultanov, M. Tikhonovsky, G. Salishchev, N. Stepanov, Microstructure and mechanical properties evolution in HfNbTaTiZr refractory high entropy alloy during cold rolling, *Adv. Eng. Mater.* (2020), <https://doi.org/10.1002/adem.202000105>.
- [30] N.Y. Yurchenko, E.S. Panina, S.V. Zhrebtsov, M.A. Tikhonovsky, G.A. Salishchev, N.D. Stepanov, Microstructure evolution of a novel low-density Ti–Cr–Nb–V refractory high entropy alloy during cold rolling and subsequent annealing, *Mater. Char.* 158 (2019), <https://doi.org/10.1016/j.matchar.2019.109980>.
- [31] S. Wang, M. Wu, D. Shu, B. Sun, Kinking in a refractory TiZrHfNb_{0.7} medium-entropy alloy, *Mater. Lett.* 264 (2020) 127369, <https://doi.org/10.1016/j.matlet.2020.127369>.
- [32] M.S. Lucas, G.B. Wilks, L. Mauger, J.A. Muñoz, O.N. Senkov, E. Michel, J. Horwath, S.L. Semiatin, M.B. Stone, D.L. Abernathy, E. Karapetrova, Absence of long-range chemical ordering in equimolar FeCoCrNi, *Appl. Phys. Lett.* 100 (2012) 251907, <https://doi.org/10.1063/1.4730327>.
- [33] C. Niu, A.J. Zaddach, A.A. Oni, X. Sang, J.W. Hurt, J.M. LeBeau, C.C. Koch, D.L. Irving, Spin-driven ordering of Cr in the equiatomic high entropy alloy NiFeCrCo, *Appl. Phys. Lett.* 106 (2015) 161906, <https://doi.org/10.1063/1.4918996>.
- [34] S. Maiti, W. Steurer, Structural-disorder and its effect on mechanical properties in single-phase TaNbHfZr high-entropy alloy, *Acta Mater.* 106 (2016) 87–97.
- [35] H. Chen, A. Kauffmann, S. Seils, T. Boll, C.H. Liebscher, I. Harding, K.S. Kumar, D.V. Szabó, S. Schlabach, S. Kauffmann-Weiss, F. Müller, B. Gorr, H.J. Christ, M. Heilmair, Crystallographic ordering in a series of Al-containing refractory high entropy alloys Ta–Nb–Mo–Cr–Ti–Al, *Acta Mater.* 176 (2019) 123–133, <https://doi.org/10.1016/j.actamat.2019.07.001>.
- [36] N.S. Stoloff, R.G. Davies, The mechanical properties of ordered alloys, *Prog. Mater. Sci.* 13 (1968) 1–84, [https://doi.org/10.1016/0079-6425\(68\)90018-2](https://doi.org/10.1016/0079-6425(68)90018-2).
- [37] N.S. Stoloff, R.G. Davies, The plastic deformation of ordered FeCo and Fe₃Al alloys, *Acta Mater.* 12 (1964) 473–485, [https://doi.org/10.1016/0001-6160\(64\)90019-7](https://doi.org/10.1016/0001-6160(64)90019-7).
- [38] R. Zhang, S. Zhao, C. Ophus, Y. Deng, S.J. Vachhani, B. Ozdol, R. Traylor, K.C. Bustillo, J.W. Morris, D.C. Chrzan, M. Asta, A.M. Minor, Direct imaging of short-range order and its impact on deformation in Ti–6Al, *Sci. Adv.* 5 (2019), eaax2799, <https://doi.org/10.1126/sciadv.aax2799>.
- [39] R. Kolli, A. Devaraj, A review of metastable beta titanium alloys, *Metals (Basel)* 8 (2018) 506, <https://doi.org/10.3390/met8070506>.
- [40] I. Weiss, S.L. Semiatin, *Thermomechanical Processing of Beta Titanium Alloys—An Overview*, 1998.
- [41] M. Abdel-Hady, K. Hinoshita, M. Morinaga, General approach to phase stability and elastic properties of β -type Ti-alloys using electronic parameters, *Scripta Mater.* 55 (2006) 477–480, <https://doi.org/10.1016/j.scriptamat.2006.04.022>.

- [42] M. Marteleur, F. Sun, T. Gloriant, P. Vermaut, P.J. Jacques, F. Prima, On the design of new β -metastable titanium alloys with improved work hardening rate thanks to simultaneous TRIP and TWIP effects, *Scripta Mater.* 66 (2012) 749–752, <https://doi.org/10.1016/j.scriptamat.2012.01.049>.
- [43] F. Sun, J.Y. Zhang, M. Marteleur, T. Gloriant, P. Vermaut, D. Laillé, P. Castany, C. Curfs, P.J. Jacques, F. Prima, Investigation of early stage deformation mechanisms in a metastable β titanium alloy showing combined twinning-induced plasticity and transformation-induced plasticity effects, *Acta Mater.* 61 (2013) 6406–6417, <https://doi.org/10.1016/j.actamat.2013.07.019>.
- [44] J. Hwang, S. Kuramoto, T. Furuta, K. Nishino, T. Saito, Phase-stability dependence of plastic deformation behavior in Ti-Nb-Ta-Zr-O alloys, *J. Mater. Eng. Perform.* (2005) 747–754, <https://doi.org/10.1361/105994905X75556>. Springer.
- [45] S. Wei, S.J. Kim, J.Y. Kang, Y. Zhang, Y. Zhang, T. Furuhashi, E. Soo Park, C.C. Tسان, Natural-mixing Guided Design of Refractory High-Entropy Alloys with As-Cast Tensile Ductility, n.D.
- [46] L. Lilensten, J.-P. Couzinié, J. Bourgon, L. Perrière, G. Dirras, F. Prima, I. Guillot, Design and tensile properties of a bcc Ti-rich high-entropy alloy with transformation-induced plasticity, *Mater. Res. Lett.* 5 (2017) 110–116, <https://doi.org/10.1080/21663831.2016.1221861>.
- [47] H. Huang, Y. Wu, J. He, H. Wang, X. Liu, K. An, W. Wu, Z. Lu, Phase-transformation ductilization of brittle high-entropy alloys via metastability engineering, *Adv. Mater.* 29 (2017) 1701678, <https://doi.org/10.1002/adma.201701678>.
- [48] L. Zhang, H. Fu, S. Ge, Z. Zhu, H. Li, H. Zhang, A. Wang, H. Zhang, Phase transformations in body-centered cubic Nb_xHfZrTi high-entropy alloys, *Mater. Char.* 142 (2018) 443–448, <https://doi.org/10.1016/j.matchar.2018.06.012>.
- [49] L. Wang, C. Fu, Y. Wu, Q. Wang, X. Hui, Y. Wang, Formation and toughening of metastable phases in TiZrHfAlNb medium entropy alloys, *Mater. Sci. Eng. A* 748 (2019) 441–452, <https://doi.org/10.1016/j.msea.2018.12.033>.
- [50] R.J. Talling, R.J. Dashwood, M. Jackson, D. Dye, Compositional variability in gum metal, *Scripta Mater.* 60 (2009) 1000–1003, <https://doi.org/10.1016/j.scriptamat.2009.02.044>.
- [51] A. Gysler, G. Lütjering, V. Gerold, Deformation behavior of age-hardened Ti-Mo alloys, *Acta Metall.* 22 (1974) 901–909, [https://doi.org/10.1016/0001-6160\(74\)90057-1](https://doi.org/10.1016/0001-6160(74)90057-1).
- [52] S.A. Mantri, D. Choudhuri, T. Alam, V. Ageh, F. Sun, F. Prima, R. Banerjee, Change in the deformation mode resulting from beta-omega compositional partitioning in a Ti-Mo alloy: room versus elevated temperature, *Scripta Mater.* 130 (2017) 69–73, <https://doi.org/10.1016/j.scriptamat.2016.11.013>.
- [53] S. Banerjee, U.M. Naik, Plastic instability in an omega forming Ti-15% Mo alloy, *Acta Mater.* 44 (1996) 3667–3677, [https://doi.org/10.1016/1359-6454\(96\)00012-2](https://doi.org/10.1016/1359-6454(96)00012-2).
- [54] J.Y. Zhang, J.S. Li, G.F. Chen, L. Liu, Z. Chen, Q.K. Meng, B.L. Shen, F. Sun, F. Prima, Fabrication and characterization of a novel β metastable Ti-Mo-Zr alloy with large ductility and improved yield strength, *Mater. Char.* 139 (2018) 421–427, <https://doi.org/10.1016/j.matchar.2018.03.031>.
- [55] W. Wang, X. Zhang, W. Mei, J. Sun, Role of omega phase evolution in plastic deformation of twinning-induced plasticity β Ti–12V–2Fe–1Al alloy, *Mater. Des.* 186 (2020) 108282, <https://doi.org/10.1016/j.matdes.2019.108282>.
- [56] O.N. Senkov, A.L. Pilchak, S.L. Semiatin, Effect of cold deformation and annealing on the microstructure and tensile properties of a HfNbTaTiZr refractory high entropy alloy, *Metall. Mater. Trans. A* 49 (2018) 2876–2892, <https://doi.org/10.1007/s11661-018-4646-8>.
- [57] O.N. Senkov, S. Rao, K.J. Chaput, C. Woodward, Compositional effect on microstructure and properties of NbTiZr-based complex concentrated alloys, *Acta Mater.* (2018), <https://doi.org/10.1016/j.actamat.2018.03.065>.
- [58] S.P. Wang, E. Ma, J. Xu, New ternary equi-atomic refractory medium-entropy alloys with tensile ductility: Hafnium versus titanium into NbTa-based solution, *Intermetallics* 107 (2019) 15–23, <https://doi.org/10.1016/j.intermet.2019.01.004>.
- [59] X. Yan, Y. Zhang, A body-centered cubic Zr50Ti35Nb15 medium-entropy alloy with unique properties, *Scripta Mater.* 178 (2020) 329–333, <https://doi.org/10.1016/j.scriptamat.2019.11.059>.